Origin of the May 1998 suprathermal particles: Solar and Heliospheric Observatory/Charge, Element, and Isotope Analysis System/(Highly) Suprathermal Time of Flight results

K. Bamert,[1] R. F. Wimmer-Schweingruber,[1] R. Kallenbach,[2] M. Hilchenbach,[3] B. Klecker,[4] A. Bogdanov,[4,5] and P. Wurz[1]

Received 3 May 2001; revised 20 August 2001; accepted 2 November 2001; published 24 July 2002.

[1] The Solar and Heliospheric Observatory/Charge, Element, and Isotope Analysis System/(Highly) Suprathermal Time of Flight ((H)STOF) mass spectrometer measures the elemental composition and the charge state distribution of ions with suprathermal energies in the range 10–4000 keV amu^{-1} from above the solar wind particle distribution up to low-energy flare particle energies. We analyze the time period around the large coronal mass ejection event on 2–3 May 1998. Using data from (H)STOF, we study the charge state distribution of He, the CNO group, and Fe. In addition, we investigate the energy dependence of the mean ionic charge state of Fe in the energy-per-nucleon range 12–100 keV amu^{-1}. Furthermore, we also report energy spectra of H^+, He^{++}, and He^+ and the variations in the elemental abundance ratios He/H, He/CNO, and Fe/CNO. These observations greatly extend the energy range in which particles associated with this time period have been measured. Because of their elevated energies, suprathermal particles are the prime seed population for further acceleration in gradual events. We identify interstellar pickup ions as an important nonsolar seed population. The observed low mean ionic charge states of Fe and the small Fe/CNO ratio are typical for large gradual events. The energy dependence of the Fe charge states may be a result of the presence of different iron populations or of the thermal history of the accelerated material. The temporal variations of Fe/CNO and He/CNO indicate a stronger confinement of low-rigidity particles at the acceleration site. *INDEX TERMS:* 2139 Interplanetary Physics: Interplanetary shocks; 2152 Interplanetary Physics: Pickup ions; 7513 Solar Physics, Astrophysics, and Astronomy: Coronal mass ejections; 7514 Solar Physics, Astrophysics, and Astronomy: Energetic particles (2114); *KEYWORDS:* IP shocks, coronal mass ejection, pickup ions, suprathermal particles, solar particle events

1. Introduction

[2] Solar particle events are generally categorized into two classes, gradual and impulsive. Gradual events are associated with coronal mass ejections (CMEs), interplanetary (IP) shocks, and type II radio bursts. Their average elemental composition reflects conditions in the solar corona. The mean charge states of all elements and the Fe/O ratio are similar to those in the solar wind. Gradual events are also called proton rich because of their large proton-to-electron ratio. Impulsive events are caused by solar flares that only last a few hours. Impulsive events are associated with type III radio bursts and short-duration X-ray emission. Their interplanetary particle fluxes are relatively low, and the heavy ions as well as ^{3}He are enriched relative to their coronal abundances. The mean charge state of Fe is significantly higher. It is generally agreed upon that the origin of the accelerated particles in the two classes is quite different. While the source region of the particles in gradual events is the fairly steady corona and the solar wind, the particles in impulsive events may be extracted from the actual active flare site at low solar altitudes. This coarse classification of solar particle events was introduced by, for example, *Reames* [1990, 1993], *Kahler* [1992, 1994], and *Gosling* [1993]. Today those two classes (gradual and impulsive) serve as starting points for more elaborated classification schemes involving mixtures of the two classes (gradual-impulsive, impulsive-gradual [*Kahler*, 1996]. The important observation for this work is that the origin of the solar energetic particle (SEP) events is imprinted in their composition, be it charge states of elements or elemental abundance ratios.

[3] We will describe measurements of low-energy particles made with the (Highly) Suprathermal Time of Flight ((H)STOF) mass spectrometer, which is part of the Charge, Element, and Isotope Analysis System (CELIAS) on board the Solar and Heliospheric Observatory (SOHO). SOHO is a project of international cooperation between the European Space Agency (ESA) and NASA. Because (H)STOF

[1]Physikalisches Institut, Universität Bern, Bern, Switzerland.
[2]International Space Science Institute, Bern, Switzerland.
[3]Max-Planck-Institut für Aeronomie, Katlenburg-Lindau, Germany.
[4]Max-Planck-Institut für extraterrestrische Physik, Garching, Germany.
[5]Now at Institut für Geophysik und Meteorologie, Technische Universität Braunschweig, Braunschweig, Germany.

0148-0227/02/2001JA900173$09.00

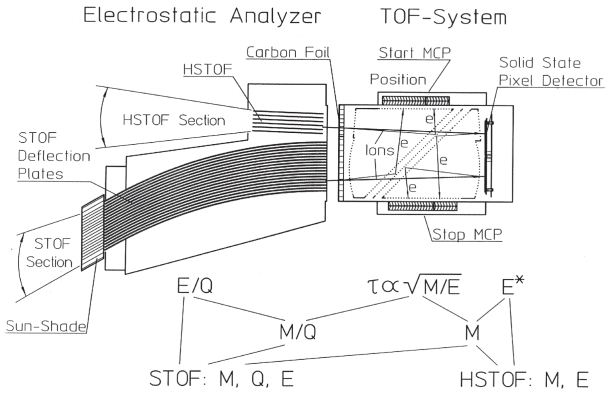

Figure 1. Schematic drawing of the Highly Suprathermal Time-of-Flight (HSTOF) sensor [from *Hovestadt et al.*, 1995].

measures particles in the energy range between the solar wind and solar energetic particles, we will mainly use the term suprathermal particles (STPs). We will discuss possible implications about the origin of suprathermal particles. (H)STOF gives data on the mass, charge, and velocity of particles in an energy range previously not accessible. This allows us to address the origins of the seed population for acceleration in gradual events.

2. The SOHO/CELIAS/(H)STOF Sensor

[4] The CELIAS instrument package aboard SOHO contains two instruments to measure the composition of suprathermal particles: the Suprathermal Time-of- Flight (STOF) and Highly Suprathermal Time-of-Flight (HSTOF) spectrometers. Both share certain instrumental and structural parts (see Figure 1) and are often referred to as one instrument, (H)STOF. STOF can measure the elemental and ionic composition in the energy-per-charge range from 35 to 660 keV e^{-1}, and HSTOF can measure the elemental composition of particles with energies per charge above 80 keV e^{-1} and energies below 80 MeV. Thus (H)STOF covers a little-explored energy range of the interplanetary plasma. Figure 2 puts (H)STOF in the context of currently flying instrumentation on SOHO and on the Advanced Composition Explorer (ACE) spacecraft, which both observed the May 1998 events. Obviously, (H)STOF bridges the gap between solar wind experiments and low- and high-energy solar energetic particle instrumentation. The STOF sensor uses electrostatic deflection, time-of-flight measurement, and the determination of the residual energy in a solid-state detector. The entrance system consists of a stack of curved deflection plates and serves as an E/q analyzer with an E/q resolution $\frac{\Delta(E/q)}{E/q} \sim 10\%$ (full width at half maximum (FWHM)). The E/q range is stepped through twice during one cycle in 120 logarithmically spaced steps (120 steps up, 120 steps down). One step takes 1.25 s, and hence a cycle takes 5 min to complete. The geometrical factor of STOF is 0.05 cm^2 sr. Adjacent to the STOF E/q analyzer there is the HSTOF entrance system that consists of a parallel plate stack, which allows only ions with energies per charge above 80 keV e^{-1} to pass to the time-of-flight section. The potential across the plates is kept fixed, and hence no E/q information is available for the charge state determination. HSTOF measures the time of flight and the residual energy in a solid-state detector to determine the mass and energy of an ion. The geometrical factor of the HSTOF entrance system is 0.22 cm^2 sr. After passing the entrance system the ions enter the time-of-flight unit through a thin carbon foil (4 μg cm^{-2}) or in the case of HSTOF through a three-layer composite silicon-lexan-carbon foil (≈28/30.5/5 nm thick). At the

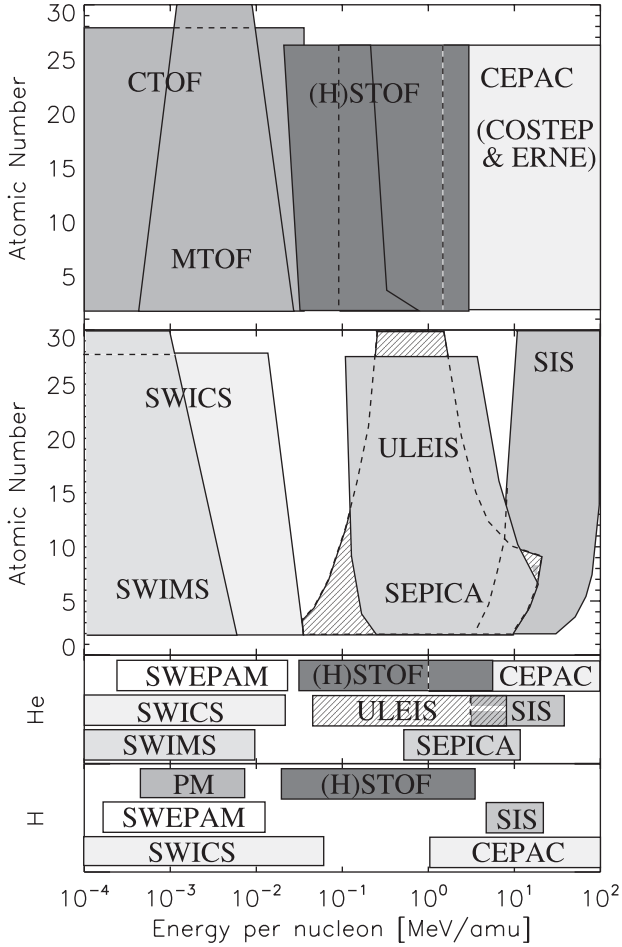

Figure 2. Energy-per-mass coverage of currently flying composition experiments on SOHO and on ACE, which observed the May 1998 events. Abbreviations and references are as follows: Charge Time of Flight (CTOF), Mass Time of Flight (MTOF), and (Highly) Suprathermal Time of Flight ((H)STOF) [*Hovestadt et al.*, 1995]; Comprehensive Suprathermal and Energetic Particle Analyzer (COSTEP) [*Müller-Mellin et al.*, 1995]; Energetic and Relativistic Nuclei and Electron Experiment (ERNE) [*Torsti et al.*, 1995]; Solar Wind Ion Composition Spectrometer (SWICS) and Solar Wind Ion Mass Spectrometer (SWIMS) [*Gloeckler et al.*, 1998]; Solar Wind Electron, Proton, and Alpha Monitor (SWEPAM) [*McComas et al.*, 1998]; Ultra Low Energy Isotope Spectrometer (ULEIS) [*Mason et al.*, 1998]; Solar Energetic Particle Ionic Charge Analyzer (SEPICA) [*Möbius et al.*, 1998]; Solar Isotope Spectrometer (SIS) [*Stone et al.*, 1998]. (H)STOF (dark shading) bridges the gap between solar wind instrumentation and energetic particle experiments.

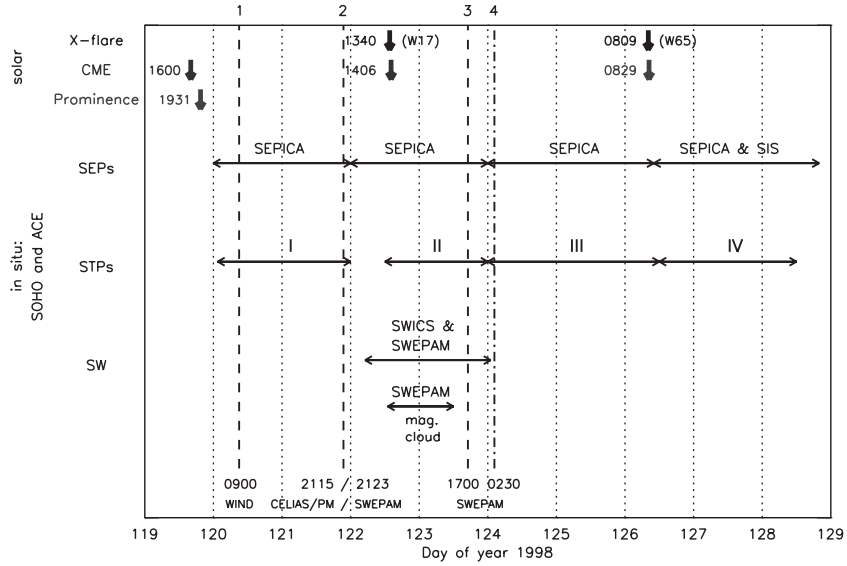

Figure 3. The May 1998 events from the Sun to $L1$ observed with optical instruments on SOHO and particle experiments on ACE and SOHO covering a wide energy range from the solar wind distribution up to solar energetic particle energies (see also Figure 2). The IP shocks are indicated by dashed vertical lines (1, 2, and 3). The interplanetary (IP) discontinuity is marked by the dash-dotted line (4). The durations of the different events are indicated by horizontal arrows. The timing information (IP shock, line 1) was taken from "Wind Interplanetary Shocks" (http://lepmfi.gsfc.nasa.gov/mfi/ip_shock.html).

end of the time-of-flight unit they reach the solid-state detectors, where the residual energy of the ions is measured. The measurements of energy per charge, time of flight, and residual energy in the solid-state detector are combined to determine uniquely the mass, charge, and the initial energy (STOF) and the mass and the initial energy (HSTOF) of an ion. The start and stop signals for the time-of-flight measurement are generated by secondary electrons emitted by the foil and the surface of the solid-state detectors, respectively. These electrons are accelerated to $\approx$1 keV by a thin wire mesh and are then deflected by an electrostatic mirror to the microchannel plates. The energy losses in the foil and in the dead layer of the solid-state detector need to be considered, since the time of flight and the energy of an ion are determined after the passage of the foil and the dead layer of the solid-state detector, respectively. The outstanding linearity and the large dynamic range of $\approx$4000 (from 20 keV up to 85 MeV) of the solid-state detectors are achieved by switching the capacitors in two gain steps (0, 1) synchronously with the E/q stepping of STOF. Owing to the partially unknown instrumental efficiencies for STOF and HSTOF, Caused, for example, by degradation of the efficiency of the microchannel plates, we limit our analysis to spectral forms and abundance ratios and do not report absolute fluxes. For the data analysis, so-called pulse height analysis (PHA) words are used, which are the most detailed data produced by (H)STOF. PHA words allow us to perform consistency checks and to disregard events in high-background (low signal-to-noise ratio) pixels of the solid-state detectors. A more detailed description of the data analysis is given in Appendix A. We have developed a model of the STOF section of the sensor which we apply to the data for analysis. It is described in Appendix B. A detailed description of the CELIAS instrument has been given by *Hovestadt et al.* [1995].

3. May 1998 Events

[5] The beginning of May 1998 saw a sequence of fairly intense SEP events and CMEs. These events were observed by an impressive number of instruments, both remote-sensing optical and in situ particle instruments. The particle instruments cover the entire energy range from solar wind to solar energetic particles. (H)STOF plays an important role in this respect, because it bridges the gap between the solar wind and the low-energy solar energetic particles, as can be seen in Figure 2. We attempt to summarize the complex sequence of events in early May 1998 in Figure 3.

[6] The timing information was taken from the International Solar Terrestrial Physics (ISTP) web site on the May 1998 events (http://www-istp.gsfc.nasa.gov/istp/events/1998may1/). Where possible, we have tried to credit the information given as personal communication. As seen from top to bottom, the events occurring at the Sun were observed with remote-sensing instruments on SOHO. With some delay, the related particle events were detected with instruments on SOHO and ACE, which are both in a halo orbit around the first Lagrangian point $L1$. Because of the velocity dispersion, the solar energetic particles arrived at $L1$ first, followed by the suprathermal particles and the solar wind. The solid horizontal arrows indicate the duration of the different events. Three interplanetary (IP) shocks are indicated by dashed vertical lines (1, 2, and 3). The IP discontinuity is marked by the dash-dotted line (4). The sequence of SEP events and CMEs begins with a halo CME observed by the Extreme Ultraviolet Imaging Telescope

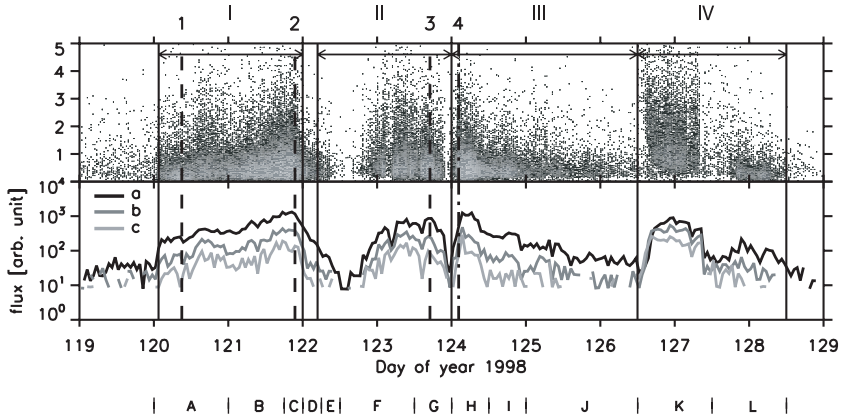

Figure 4. Overview of the May 1998 time period. In the top panel, each dot corresponds to a He particle detected by HSTOF. Its measured energy is plotted versus time. In the bottom panel the He fluxes are shown in arbitrary units (hourly averages) in three energy ranges: (a), 0.25–0.5 MeV amu^{-1}; (b), 0.5–0.75 MeV amu^{-1}; (c), 0.75–1.0 MeV amu^{-1}. The periods indicated by vertical solid lines are the four STP events (I–IV) observed with (H)STOF during this time period. The dashed vertical lines mark the IP shocks on 30 April at 0900 UT (line 1), on 1 May at 2115 UT (line 2), and on 3 May at 1700 UT (line 3), respectively. The dash-dotted line indicates the IP discontinuity on 4 May at 0230 UT. See Table 2 and Figures 5 and 6 for more details.

(EIT) on SOHO on 29 April (day of year (DOY) 119) at 1600 UT and at 1658 UT by the Large Angle and Spectrometric Coronagraph (LASCO) on SOHO (S. Paswaters, personal communication, 1998). Later on, LASCO observed an erupting prominence at 1931 UT. A few hours later (at ~0130 UT on DOY 120), SOHO/ CELIAS/ (H)STOF observed the onset of a gradual STP event. Similar observations were made by *Klecker et al.* [1999]. The Proton Monitor (PM), which measures bulk solar wind properties on SOHO and is part of the CELIAS sensor package, detected a shock driven by the 29 April CME on 1 May (DOY 121) at 2115 UT (F. M. Ipavich, personal communication, 1998). This shock was also observed on ACE at 2123 UT [*Skoug et al.*, 1999]. The relative timing of the EIT/LASCO observations implies a shock travel time to $L1$ at ~1 AU of ~53 hours, corresponding to an average shock travel speed of ~790 km s^{-1}. The associated CME was observed between 0500 UT on 2 May (DOY 122) and 0100 UT on 4 May (DOY 124) [*Skoug et al.*, 1999]. Because ACE is also in a halo orbit around $L1$, the relative time differences between ACE and SOHO are small (order of ~10 min). The identification of the CME was primarily based on the presence of counterstreaming electrons and on the observation of a magnetic cloud during a subinterval during the entire CME. In this way the sensors on ACE ideally complement the optical instruments on SOHO. Another X-class flare and halo CME were observed on 2 May at 1340 and 1406 UT, respectively (S. Stezelberger, personal communication, 1998), which may have been associated with the IP discontinuity at $L1$ on 4 May (DOY 124) at 0230 UT. In the solar wind a large increase in plasma speed, temperature, and field strength was measured [*Skoug et al.*, 1999]. At the same time the Polar spacecraft observed an extreme compression of the magnetosphere [*Russell et al.*, 2000]. On 6 May (DOY 126) an X-class flare was detected at 0809 UT, and at 0829 UT a very wide and fast CME was seen (S. Paswaters, personal communication, 1998). Both events were magnetically well connected to the Earth. The corresponding SEP data showed characteristics of both impulsive and gradual and a strong velocitiy dispersion [*Popecki et al.*, 1999]. The velocity dispersion will be discussed in more detail in this work. During this time no magnetic clouds or IP shocks were noted [*Popecki et al.*, 1999]. A more complete description of the events is given in Figure 3, and the temporal evolution can be seen in Figure 4.

[7] In the top panel we have plotted the measured energy of each He particle detected with HSTOF (gain 0: 0.04–7 MeV) versus the time of its detection. In the bottom panel the hourly averages of the He fluxes in arbitrary units in three energy ranges (a, 0.25–0.5 MeV amu^{-1}; b, 0.5–0.75 MeV amu^{-1}; c, 0.75–1.0 MeV amu^{-1}) are shown. The times of the observed STP events on DOY 120–121, on DOY 122–123, and on DOY 126–128 are indicated by vertical solid lines and marked with roman numerals, I–IV. The IP shocks observed on 30 April (DOY 120) at 0900 UT (line 1), on 1 May (DOY 121) at 2115 UT (line 2), and on 3 May (DOY 123) at 1700 UT (line 3) are indicated by dashed vertical lines. The dash-dotted line marks the IP discontinuity on 4 May (DOY 124) at 0230 UT (line 4). The STP and SEP events in the May 1998 time period are complicated to analyze because of the multiple source populations that need to be considered. The application of the usual argument that the composition of SEPs in gradual events is approximately the same as that of the ambient solar wind breaks down in these events, because the solar wind itself exhibited a most unusual composition during this time period. For the solar wind energy range, *Gloeckler et al.* [1999] have reported mixtures of high and low charge states for all heavy solar wind ions, as well as for He. Also in the solar wind energy range, *Skoug et al.* [1999] measured a prolonged He^+ enhancement for an interval of more than 24 hours. The solar wind was also strongly mass fractionated; relative to O, He was enriched by a factor of ~10, and Fe was enriched by a factor of ~2. Furthermore, ^{3}He was enhanced by a factor of ~7 [*Gloeckler et al.*, 1999; *Ho et al.*, 2000]. Evidently, such an unusual composition complicates the analysis of the events, because material that

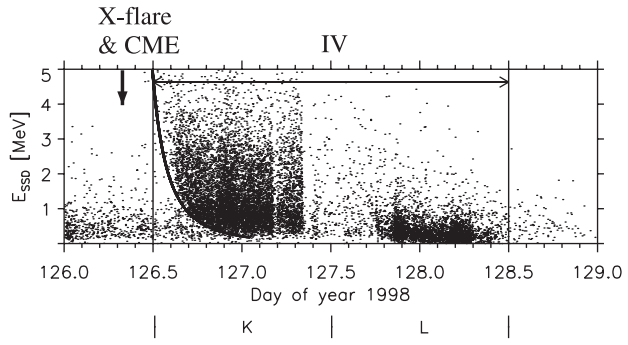

Figure 5. HSTOF data for event IV: detail from top panel in Figure 4. SOHO/ Extreme Ultraviolet Imaging Telescope (EIT) observed on 6 May at 0809 UT an X-class flare, and SOHO/ Large Angle and Spectrometric Coronagraph (LASCO) observed at 0829 UT a wide and fast coronal mass ejection (CME). The suprathermal particle (STP) event exhibited a strong velocity dispersion. The solid curve is calculated with $s = 1.275 \pm 0.25$ AU.

was accelerated out of the solar wind associated with the 2–3 May CME will have unusual composition and might be mistaken to be of impulsive nature. This is especially true for the IP shock on 3 May at 1700 UT and the IP discontinuity on 4 May at 0230 UT shown in Figure 4. The onset times of the STP events are obvious, as is the fact that the four events are quite different in nature. While the events I and III commence abruptly and show no velocity dispersion, event II shows a slow increase in the number of high-energy particles, as well as some intervals that seem to be disconnected from the source of the STPs. Such intervals are also seen in event III. On the other hand, event IV also exhibits a clear velocity dispersion at its onset, with the high-energy particles arriving before the lower-energy ones. We show a blowup of event IV in Figure 5.

[8] For a nonrelativistic particle of mass m and kinetic energy E, the travel time t along a magnetic field line of length s from near the Sun to $L1$ is given by $t = s\sqrt{m/2E}$. From HSTOF data we found $s = 1.275 \pm 0.25$ AU. We have plotted the corresponding velocity curve in Figure 5. There seems to be an indication of an additional event toward the end of DOY 127, although statistics are insufficient to ascertain this claim. It is obvious that it is not magnetically connected with the preceding event. The IP shock on 1 May (DOY 121) and the IP discontinuity on 4 May (DOY 124) clearly accelerated a large number of particles to high energies. Because the flux of STPs peaks near the IP shock and the IP discontinuity, it appears that they have been accelerated locally (see Figure 4). We will investigate this aspect further below. As we will show, the STPs exhibited unusual charge state composition throughout the period of interest. STPs, by virtue of their enhanced energy, are the prime source population for further acceleration in gradual events. Obviously, unusual composition in the STPs will leave a signature in SEPs that may be difficult to interpret without the knowledge of STP composition.

4. Results

[9] A summary of the (H)STOF results for the May 1998 period (from DOY 119 until DOY 129) is given in Figure 6. The four events (I–IV) and the magnetic cloud portion of the 2–3 May CME (event II) are indicated by vertical solid lines. The dashed vertical lines mark the IP shocks on 30 April at 0900 UT (line 1), on 1 May at 2123 UT (line 2) driven by the 29 April CME, and on 3 May at 1700 UT (line 3). The dash-dotted line denotes the IP discontinuity on 4 May at 0230 UT (line 4). The thick horizontal bar indicates the time of enhanced He^+ in the solar wind [textit *Skoug et al.*, 1999; *Gloeckler et al.*, 1999]. We show from top to bottom, He^{++}/He, He^{++}, and He^+ fluxes in arbitrary units, the He/H elemental abundance ratio, the H and He fluxes in arbitrary units, He, CNO, and Fe fluxes in arbitrary units, and the elemental abundance ratios of Fe and He relative to the sum of C, N, and O. The coronal abundance ratios of He/H, Fe/CNO, and He/CNO [*Reames*, 1999] are indicated by dashed lines. The energy-per-mass ranges of the four ratios are listed in Table 1.

[10] Open symbols in the ratios denote 6-hour averages, while solid symbols are averages over the periods A–L as indicated at the bottom of the plot. The typical uncertainties of the fluxes are smaller than the plotted symbols. The means and statistical errors of the averages over the periods A–L for the four ratios are summarized in Table 2.

[11] One of the unusual features observed in the suprathermal particles during the May 1998 time period is the charge state composition of He at the onset of event I. The flux of He begins to rise at the beginning of DOY 120 (Figure 6e). With STOF we observe both He^{++} and He^+ (Figure 6b), with the flux of He^+ exceeding that of He^{++}. The fluxes of STP He peak near the IP shock (line 1) observed at Wind around 0900 UT. The He^+ flux drops by about a factor of 2 and stays at a constant level until it increases again in association with the IP shock (line 2) observed by the SOHO/CELIAS/PM at 2115 UT on DOY 121 (F. M. Ipavich, personal communication, 1998). He^{++}, on the other hand, initially drops by a smaller factor than He^+ and then increases around the beginning of DOY 121. That He^+ and He^{++} do not behave in the same manner on DOY 120 is reflected in the charge state composition of He. On DOY 120 and in the energy range covered by STOF, He^+ accounts for ~50% of all He, while the He^{++}/He ratio rises to around unity on DOY 121. Thus it appears that the He charge state composition was rather unusual during period A (see Figure 6). We will investigate the energy dependence shortly.

4.1. Elemental Composition

[12] To reduce the statistical uncertainties we used HSTOF data to calculate the elemental abundance ratios He/H, He/CNO, and Fe/CNO. The variations in 6-hour averages of these abundance ratios are shown in Figure 6. During event I and until the onset of event II (periods A–E), the Fe/CNO ratio is consistent with coronal abundances. No significant enhancement in association with the IP shock on DOY 121 (period C) was observed. At the onset of event I the He/CNO ratio is enhanced by a factor of 2 and then drops successively by a factor of 3.5. After the IP shock on DOY 121 (period D) it rises to coronal abundances. During period A the He/H ratio is consistent with the coronal abundance ratio. In the second half of event I (period B), He/H rises by a factor of 1.75. It thus shows the inverse behavior of He/CNO, indicating that the He ions behave anomalously with

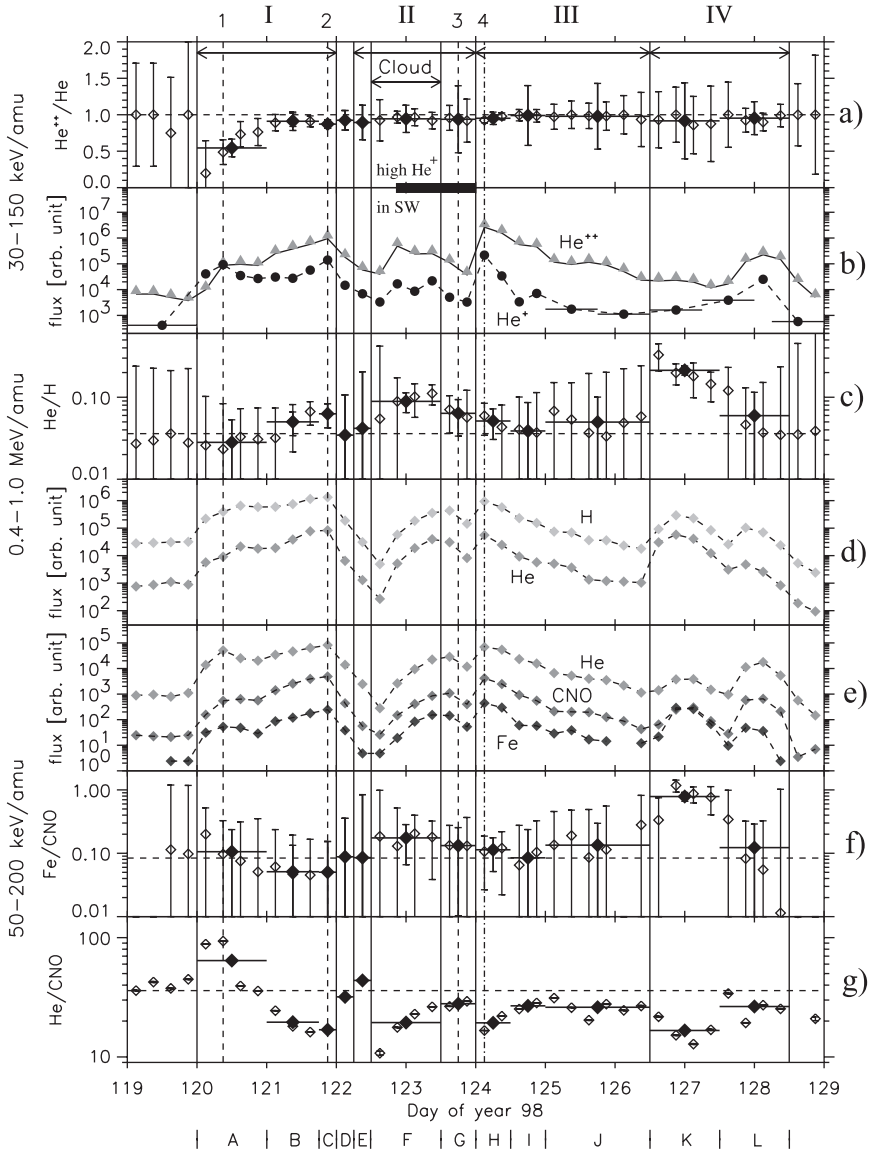

Figure 6. (a–g) Overview of the May 1998 time period. Indicated by the solid vertical lines are the four events (I–IV) and the magnetic cloud portion of the 2 May CME (event II). The dashed vertical lines mark the IP shocks on 30 April at 0900 UT (line 1), on 1 May at 2115 UT driven by the 29 April CME (line 2), and on 3 May at 1700 UT (line 3). The dash-dotted line denotes the IP discontinuity on 4 May at 0230 UT (line 4). The thick horizontal bar indicates the time of enhanced He^+ in the solar wind [*Skoug et al.*, 1999; *Gloeckler et al.*, 1999]. From top to bottom we have He^{++}/He, He^{++}, and He^+ fluxes in arbitrary units (30–150 keV amu^{-1}), the He/H elemental abundance ratio, the H and He fluxes in arbitrary units (0.4–1.0 MeV amu^{-1}), He, CNO, and Fe fluxes in arbitrary units, and the elemental abundance ratios of Fe and He relative to the sum of C, N, and O (50–200 keV amu^{-1}). The coronal abundance ratios of He/H, Fe/CNO, and He/CNO [*Reames*, 1999] are indicated by dashed lines. Open symbols in the ratios denote 6-hour averages, while solid symbols are averages over the periods A–L. The typical uncertainties of the fluxes are smaller than the plotted symbols. The reason for not giving absolute fluxes is detailed in the text. See Table 2 for detailed timing information.

respect to H or CNO. After the IP shock on DOY 121, He/H drops to coronal abundances. For all three ratios, significant changes are observed during the magnetic cloud portion of event II (period F). While He/CNO is depleted by a factor of 2.3 just around the beginning of the magnetic cloud (period F) and then returns to coronal abundances, Fe/CNO is enhanced by a factor of 2 during the whole period F and then decreases until the end of DOY 123. The He/H ratio is consistent with coronal abundances at the onset of event II. It rises during the magnetic cloud portion by a factor of 3 to drop again successively toward the end of period I to the coronal abundance ratio. The IP discontinuity (line 4) in the beginning of DOY 124 did not affect the behavior of the He/H and Fe/CNO ratios. In contrast, the He/CNO ratio is

Table 1. Energy-Per-Mass Ranges for He^{++}/He Derived From STOF, and He/H, He/CNO, and Fe/CNO Derived From HSTOF

	MeV amu^{-1}
He^{++}/He	0.03–0.15
He/H	0.4–1.0
Fe/CNO	0.05–0.2
He/CNO	0.05–0.2

initially depleted by a factor of 2 and then rises to coronal abundances until the end of DOY 124. Event IV consists of two parts, one with both high- and low-energy particles (period K) and one with only low-energy particles (period L). Period K exhibited strong velocity dispersion as we have shown in Figure 5, as well as an enrichment in heavy ions. Compared with their coronal values, He/CNO is depleted by a factor of 2, and He/H and Fe/CNO are enhanced by a factor of 6 and 9, respectively. He/H as well as Fe/CNO reach their highest values around the onset of the event and then drop successively toward the end of event IV to coronal abundances. The He/CNO ratio shows the inverse behavior. It is depleted by a factor of 2 during the first half of event IV (period K) and rises in the second half (period K) by a factor of 1.5.

4.2. Spectra

[13] In Figure 7 we show the differential fluxes for H, He^{++}, and He^{+} (STOF) and H and He (HSTOF) for the first half of event I (period A, top panel), the magnetic cloud of event II (period F, middle panel) and the time around the IP discontinuity (period H, bottom panel). The uncertainties (statistical and systematical) are generally smaller than the plotted symbols. Because of unknowns in the degradation of efficiencies of the start and stop microchannel plates (see section A2), we do not give any absolute values for the fluxes. However, this degradation does not influence the determination of energy spectra. The microchannel plates only detect the electrons emitted by the foils and the solid-state detectors, respectively. This does not introduce an energy dependence, and we are confident that the spectral shapes reported here are accurate. Period A shows unusual behavior in the spectra of He as can be seen in Figure 7. He^{+} is as abundant as He^{++} at the lowest energies measurable with STOF, and the spectrum of He^{++} is nearly flat below 200 keV amu^{-1}.

[14] We have fitted the spectra of He^{++} and He^{+} for periods A and H using the expression given by *Ellison and Ramaty* [1985]:

$$\frac{dJ}{dE} = N_0 \cdot \left(\frac{E}{m}\right)^{-\gamma} \cdot \exp\left(-\frac{E}{E_0}\right), \quad (1)$$

where the spectral index, γ, the normalization, N_0, and thee-folding energy per mass, E_0, are free parameters. These fits are shown in Figure 7.

[15] The different energy dependence of the spectra results in a rather strong energy dependence of the He charge state ratio. In Figure 8 we have plotted the ratio of He^{++}/He versus E/m both for the data and for the ratio of the spectral fits. We show this ratio for the three periods A, F, and H (from top to bottom) because they illustrate an important point of this paper. For period A we have binned three data points to reduce the statistical uncertainties. All original data points follow the trend of the model fit. During period A, at the lowest energies accessible to STOF, He^{++} accounts for only ~40% of all He, which is an unusually low value. The He^{++}/He ratio increases with increasing energy. The other periods do not exhibit this unusual behavior. In period F the spectra show a decrease in intensity for $E/m \leq 60$ keV amu^{-1} for He^{+} and $E/m \leq 90$ keV amu^{-1} for He^{++}, respectively. The He^{++}/He ratio increases slowly from 0.9 for lower energies to ~1 for energies above 100 keV amu^{-1}. In contrast, in period H, hard spectra were observed with spectral indices of ~3 for H^{+} and ~2 for He^{++}. No energy dependence is seen in the He^{++}/He ratio within the experimental uncertainty, and He^{+} accounts for only 5% of all He over the whole energy range.

4.3. Charge State Composition

[16] Observations at higher energies, i.e., in the solar energetic particle energy range (~0.1–100 MeV amu^{-1}), exhibit a trend for charge states of all elements to increase with energy [e.g., *Cohen et al.*, 1999b; *Mazur et al.*, 1999; *Möbius et al.*, 1999b]. With STOF we investigate the Fe charge states in the energy range above the solar wind. We compare the mean charge states and the width of the distribution in two energy ranges in Figure 9.

[17] We show the Fe charge states summed over periods E–G (event II) for the energy ranges 12–50 keV amu^{-1} (top panel) and 50–100 keV amu^{-1} (bottom panel). The solid and

Table 2. Mean and Statistical Uncertainties for the Averages Over the Periods A–L[a]

DOY	Period	He^{++}/He	He/H	Fe/CNO	He/CNO
120.00–121.00	A	0.545 ± 0.121	0.028 ± 0.025	0.106 ± 0.130	64.236 ± 0.047
121.00–121.75	B	0.911 ± 0.127	0.050 ± 0.016	0.051 ± 0.082	19.570 ± 0.025
121.75–122.00	C	0.872 ± 0.058	0.063 ± 0.021	0.050 ± 0.103	16.909 ± 0.032
122.00–122.25	D	0.924 ± 0.134	0.035 ± 0.072	0.088 ± 0.268	31.891 ± 0.101
122.25–122.50	E	0.894 ± 0.263	0.042 ± 0.162	0.085 ± 0.756	43.779 ± 0.275
122.50–123.50	F	0.944 ± 0.187	0.089 ± 0.024	0.175 ± 0.109	19.421 ± 0.054
123.50–124.00	G	0.938 ± 0.460	0.064 ± 0.030	0.132 ± 0.122	27.929 ± 0.054
124.00–124.50	H	0.951 ± 0.085	0.051 ± 0.021	0.114 ± 0.062	19.329 ± 0.026
124.50–125.00	I	0.989 ± 0.410	0.039 ± 0.047	0.085 ± 0.152	26.813 ± 0.055
125.00–126.50	J	0.979 ± 0.451	0.050 ± 0.051	0.134 ± 0.162	26.096 ± 0.071
126.50–127.50	K	0.916 ± 0.521	0.213 ± 0.027	0.786 ± 0.125	16.674 ± 0.077
127.50–128.50	L	0.953 ± 0.226	0.060 ± 0.055	0.123 ± 0.167	26.479 ± 0.057

[a] The energy ranges of the ratios are given in Table 1. See also Figure 6.

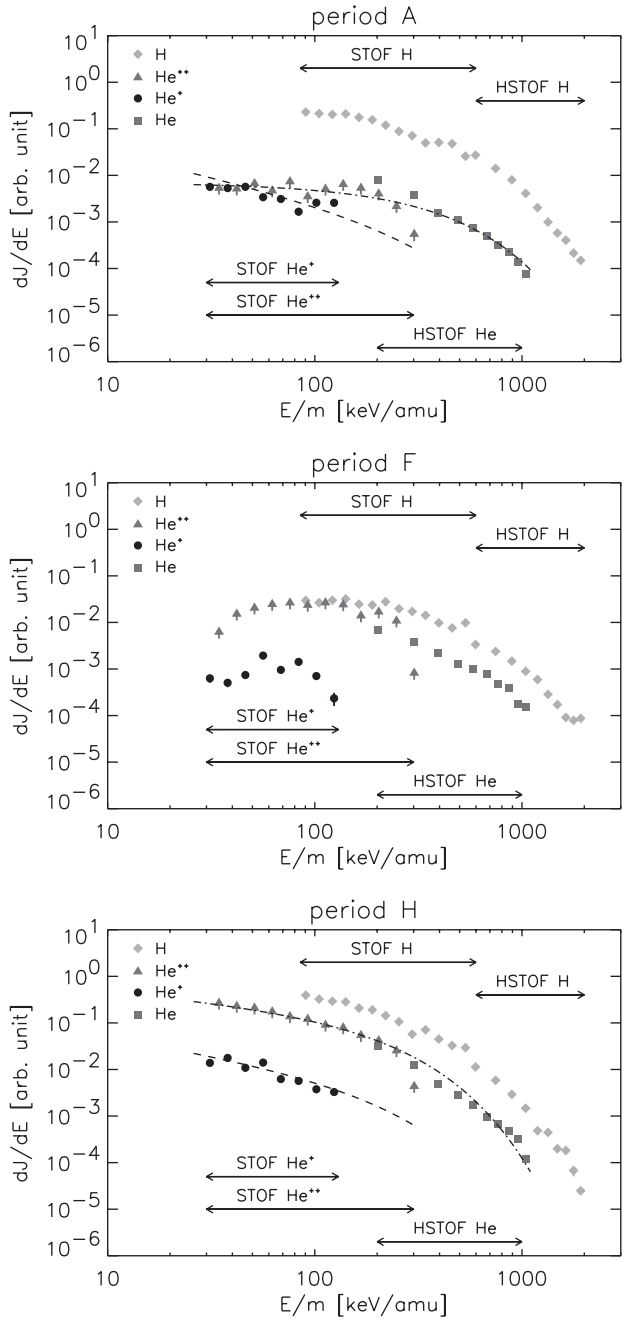

Figure 7. Differential fluxes for H, He^{++}, and He^{+} (STOF) and H and He (HSTOF) for three different periods. From top to bottom are the first half of event I (period A), which shows large He^{+} abundance, the magnetic cloud of the event II (period F), and the time around the IP discontinuity on 4 May (period H). We have fitted the spectra of He^{+} (dashed line) and He^{++} (dash-dotted line) for period A and H using equation (1).

dashed lines denote the mean charge state $\langle q \rangle$ for the lower and the higher energy range, respectively. The shaded areas cover the range $\langle q \rangle \pm \sigma$. We have plotted the weighted arithmetic mean charge state only. It agrees well with the statistically more robust median charge state. In Figure 10 we show the whole time period from DOY 119 until DOY 129 using the same plotting symbols as in Figure 9.

[18] Since the Fe fluxes are generally low with exception during periods C and H, we summed the Fe charge states over two or three periods. Period D is omitted because it contains insufficient counts to derive a meaningful result. The mean charge states and the standard deviations, σ, are listed in Table 3.

[19] During event I (periods A–C) the distribution is narrow, and mean charge states in both energy ranges are

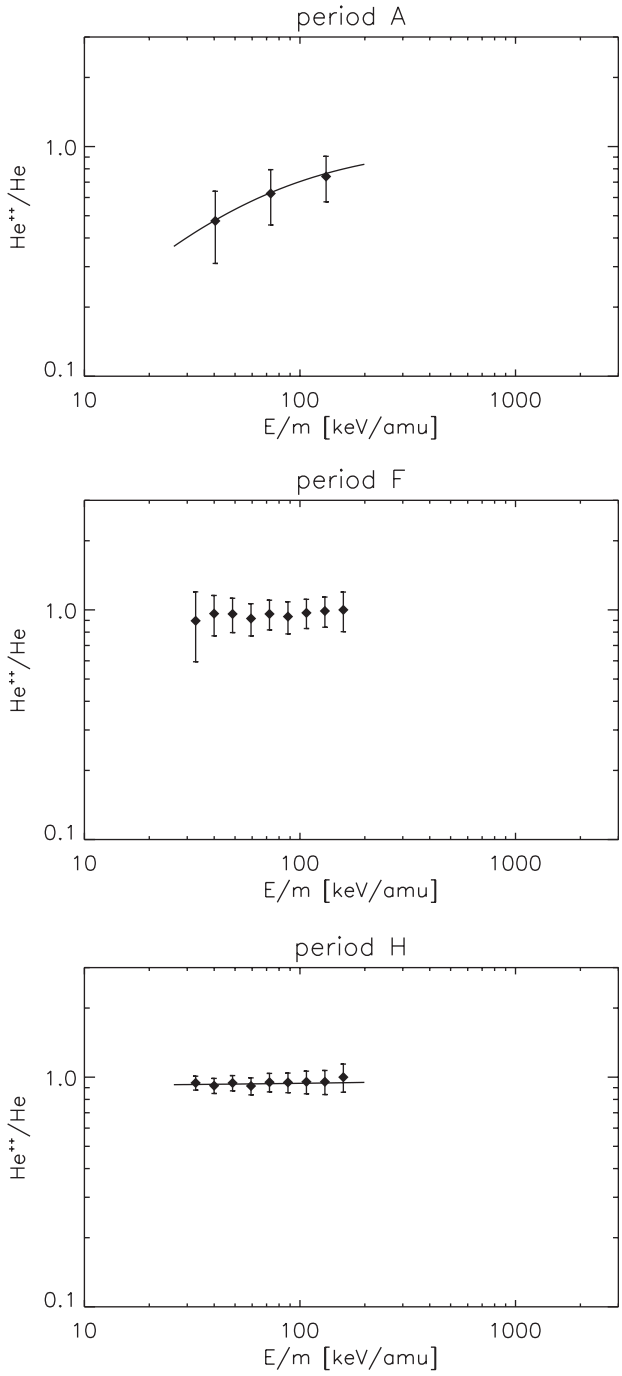

Figure 8. Energy dependence of the He^{++}/He ratio in the energy per nucleon range 30–150 keV amu^{-1} for the periods A, F, and H (from top to bottom). While period A exhibited a significant energy dependence, the He^{++}/He ratio is approximately constant in the periods F and H. The curves are the ratios of the spectral fits (see Figure 7).

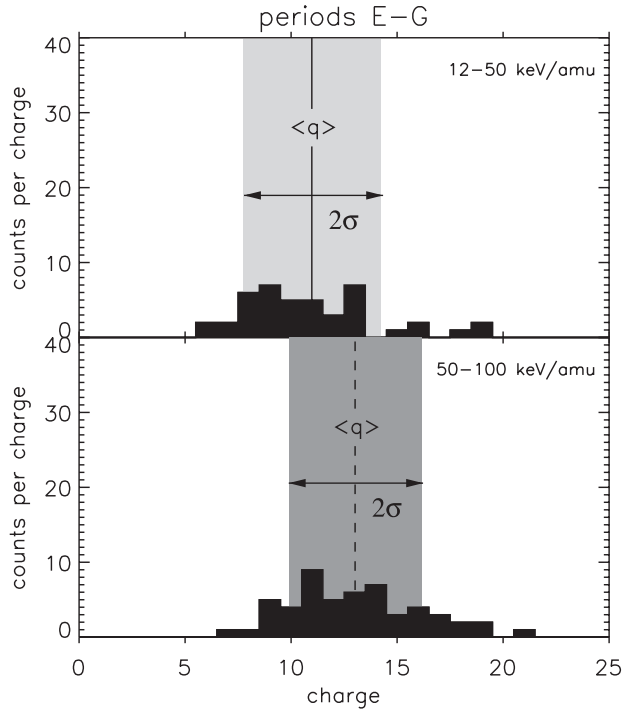

Figure 9. The Fe charge states accumulated over the periods E−G (event II). The solid and dashed lines denote the mean charge state $\langle q \rangle$ for (top) 12−50 keV amu^{-1} and (bottom) 50−100 keV amu^{-1}, respectively. The shaded areas cover the range $\langle q \rangle \pm \sigma$. The iron charge states in the higher energy range tend to be somewhat higher.

low (∼10), similar to the solar wind as expected for gradual events, and do not depend on the energy. In contrast, events II and IV (periods E−G and K and L) show a clear energy dependence and a wider distribution. The mean charge states in the higher energy range are ∼2 units larger. The wide distribution detected during event II persists at least until the end of 5 May (DOY 125). During event III the mean charge states are high (∼13.5) and independent of the energy.

5. Discussion

[20] Energetic particles associated with CMEs are known to be accelerated at shocks driven by the CME material moving away from the Sun with speeds up to 1000 km s^{-1} [e.g., *Gosling*, 1993; *Kahler*, 1994; *Reames*, 1999]. The (H)STOF sensor offers the opportunity to observe particles with energies close to the assumed injection threshold for first-order Fermi acceleration and to measure their elemental abundances and charge state composition. Variations in these abundances can occur for at least five reasons: (1) The bulk densities at the acceleration site may vary, (2) the injection efficiency into the acceleration process depends on the velocity distribution of the species, (3) the acceleration efficiency depends on mass per charge, A/Q, (4) the escape out of the acceleration volume depends on particle rigidity, and (5) the interplanetary propagation depends on the particle rigidity.

Table 3. Mean Charge States of Fe and the Standard Deviations, σ, in the Two Energy Ranges as Shown in Figure 10

	12−50 keV amu^{-1}		50−100 keV amu^{-1}	
	$\langle q \rangle$	σ	$\langle q \rangle$	σ
A+B	9.65	1.57	10.00	1.86
C	9.78	0.67	9.93	1.59
E−G	10.98	3.25	13.01	3.12
H	13.05	3.22	13.09	3.18
I+J	14.08	3.08	13.56	4.26
K+L	9.13	0.99	11.25	5.26

[21] We begin the discussion of the May 1998 time period with event IV because it is a classical example of a gradual event. Event IV shows a temporal variation of the He/CNO and the Fe/CNO abundance ratios in form of a general anticorrelation of their deviations from coronal abundance ratios but also differences and delays in their deviations. This behavior is compatible with a stronger confinement at the acceleration site of low-rigidity particles. Higher-rigidity particles escape from the shock acceleration region and can be detected by (H)STOF even when the shock is far away from the spacecraft, whereas the lower-rigidity particles are only observed during times close to the passage of the shock and the subsequent, shock-heated material. The ejecta material is not expected to have been processed by the shock. Because of its higher A/Q ratio, Fe escapes the shock region more easily than CNO, which in turn escapes more easily than He. In general, any abundance ratio of high-rigidity to low-rigidity ions, including He/H, should behave like Fe/O at the same velocity; that is, after an initial rise at the onset of the event, it should decline.

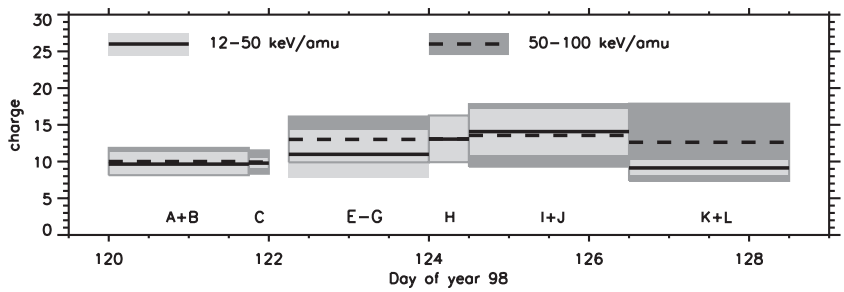

Figure 10. The same plotting symbols as in Figure 9. Since the Fe fluxes are generally low with exception of periods C and H, we accumulated the data over two or three periods as indicated at the bottom of the plot. The mean charge states $\langle q \rangle$ and the standard deviations σ for the two energy ranges are summarized in Table 3. There is an indication of an energy dependence in the iron charge states for the periods E−G (event II) and K + L (event IV).

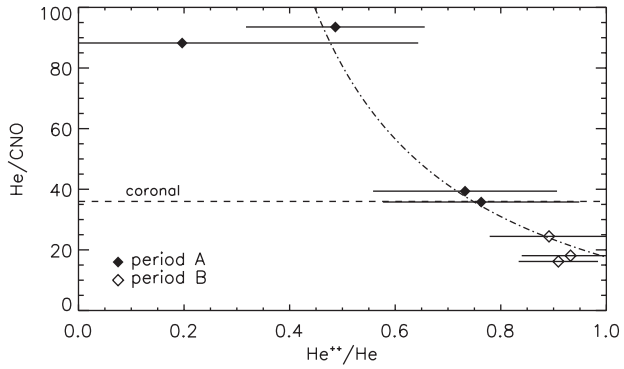

Figure 11. He/CNO versus He^{++}/He for the periods A (solid diamonds) and B (open diamonds). The dash-dotted curve shows the expected functional form and is for illustration only. The dashed line denotes the coronal value of the He/CNO ratio [*Reames*, 1999].

This behavior was observed for the 6 May event (event IV) in the energy range of HSTOF and also at higher energies [*von Rosenvinge et al.*, 1999]. However, earlier measurements, for example, by *Mason et al.* [1983] and *Tylka et al.* [1999], show a different behavior. While Fe/O abundances quickly rise above the coronal abundances and then slowly decline, He/H initially drops below the coronal ratio and then rises. This is explained by resonant wave-particle interaction of the different species with waves generated by accelerated protons. The effect is stronger for larger events because then there is a higher energetic proton flux to generate the instability that drives the waves [*Ng et al.*, 1999; *Reames et al.*, 2000].

[22] In event I we observe a behavior that differs somewhat from the two sketched behaviors. Fe/CNO remains approximately constant at the coronal value, while He/CNO is well above coronal values during the passage of the shock (line 1) and then drops to very low values before it rises again to coronal values after the passage of the shock (line 2). He/H reaches its highest value around the passage of the shock (line 2). At first sight this might seem to imply a rigidity-dependent confinement where both H and He remain confined close to the acceleration site while Fe and CNO leak out. However, such a process would have to exhibit a sharp cutoff in rigidity to handle He so differently from CNO, which has A/Q values close to He^{++}. Moreover, a substantial fraction of the He in period A is in the form of He^{+}, which has a rigidity more similar to Fe than to H. In our opinion, this rules out a rigidity-dependent confinement as an explanation. The same argument applies to A/Q-dependent acceleration. Thus, in view of the composition-altering processes mentioned above, we are left with the possibilities that the overabundance of He is due to a preferred injection of He^{+} into the suprathermal particle population or that He^{+} itself was more abundant at the acceleration site. In Figure 11 we show the He/CNO ratio as a function of He^{++}/He for period A and period B. The dashed line denotes the coronal value of the He/CNO ratio. The expected functional form for He/CNO versus He^{++}/He for a varying He^{+} abundance is indicated by the dash-dotted curve and is for illustration only. Obviously, the behavior of He^{++}/He and He/CNO in event I can be explained by a strongly varying contribution to He by singly ionized He. If preferential injection of high A/Q species is the reason for the observed relation between He^{++}/He and He/CNO, then this should be reflected in Fe/CNO. However, the statistical uncertainties are too large to substantiate this point.

[23] Event II at first shows behavior similar to that of event IV as all flux ratios of higher-to-lower rigidity particles are enhanced. Right at the shock (line 3 in Figure 4) He and H again appear to be more enriched as outlined for event I. Event II exhibits one additional particularity: During the magnetic cloud the spectra of He^{++} and He^{+} show characteristic knees and a decrease in intensity toward lower energies. He particles accelerated close to the Sun may penetrate more deeply into the cloud if they have higher energies. Thus the magnetic cloud appears to serve as an effective barrier against the low-energy portion of the suprathermal particles. No energy dependence of the He^{++}/He ratio is observed. In Figure 12 we compare the differential rigidity spectra of He^{++} and He^{+} for periods A and H. Acceleration at the strong IP discontinuity on 4 May, i. e., period H, approximately produces power law spectra both for He^{++} and He^{+} in the immediate vicinity of the discontinuity. The He ions are accelerated to the same velocity or energy per nucleon. The He^{++}/He ratio is therefore independent of energy (Figure 8). On the other hand, the He^{+} spectrum looks quite different from the He^{++} spectrum for period A. As we have already mentioned, the escape from the shock depends upon the rigidity of an ion, i.e., upon its charge-to-mass ratio. This

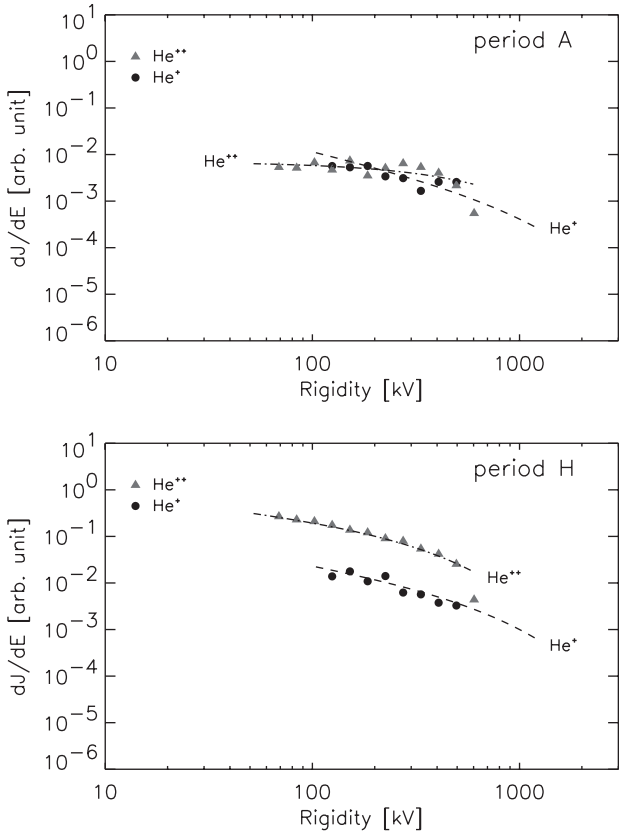

Figure 12. The differential rigidity spectra of He^{++} and He^{+} for (top) the first half of event I and (bottom) the time around the strong IP discontinuity on 4 May.

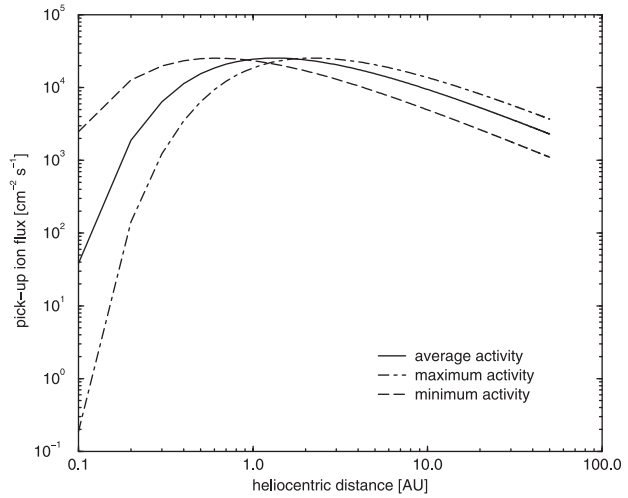

Figure 13. Flux of interstellar He pickup ions (PUIs) in the heliosphere. The three model curves correspond to the flux at solar activity minimum (dashed), maximum (dash-dotted), and the flux for average ionization rates (solid). Fluxes were calculated according to *Vasyliunas and Siscoe* [1976].

rigidity-dependent escape from the shock region may explain the shape of the He^{++} spectrum. During period A the spectrum of the lower-rigidity He^{++} is flattened more at lower rigidities than that of the higher-rigidity He^{+}. The shape of the He^{+} spectrum is still more similar to a power law, which indicates local acceleration as observed in period H. He^{++} may consist of two populations, both of solar origin: (1) locally accelerated particles at the IP shock on 30 April and (2) particles from the 29 April CME accelerated close to the Sun.

[24] The origin of He^{+} deserves a separate discussion. Using the energies (50 keV amu^{-1}) of the He^{+} particles to calculate when they left the Sun, we find that they would have had to leave the Sun a few hours before the prominence eruption on 29 April (DOY 119). At higher energies (E >100 keV amu^{-1}), where travel times are consistent with a solar origin, He^{+} accounts for only a few percent of the total He flux. Therefore we propose that there are at least two populations in event I, one possibly of solar origin with a low fraction of He^{+} and one nonsolar component with high He^{+} abundances. He^{+} in the solar wind is extremely rare [*Zwickl et al.*, 1982] and generally associated with CMEs [*Schwenn et al.*, 1980; *Fenimore*, 1980; *Ipavich et al.*, 1986]. An unusually high He^{+} abundance in the solar wind was associated with the 2–3 May CME. Measurements of particles in the solar wind energy range [*Gloeckler et al.*, 1999; *Skoug et al.*, 1999] show a dramatic increase in the abundance of He^{+} during the second half of the 2 May CME. A comparable enhancement is not seen in the accelerated particles observed with STOF. In fact, the abundance of He^{+} with respect to He^{++} is consistent with a constant value throughout the time period investigated, with the exception of the first half of event I (period A), which is more than 2 days before the enrichment of He^{+} in the solar wind. The enhancement of He^{+} in the solar wind was observed to continue beyond the magnetic cloud portion of the 2 May CME, well into the region disturbed by the IP discontinuity detected on 4 May 1998 [*Skoug et al.*, 1999]. That discontinuity was very effective at accelerating particles. The fluxes of suprathermal particles peaked during this time. Nevertheless, no enhancement of He^{+} is observed in our data. This is a strong indication that the suprathermal He^{+} particles are not accelerated out of the solar wind. This phenomenon has been known from the observations of the He^{+}/He^{++} ratio in suprathermal particles associated with corotating interaction regions at 1 AU [*Hilchenbach et al.*, 1999; *Chotoo et al.*, 2000] and at 5 AU [*Gloeckler et al.*, 1994]. Unless there is a constant background of solar suprathermal He^{+} present in the inner heliosphere (similar to the energetic $^{3}He^{++}$ population postulated by *Mason et al.* [1999]), there does not appear to be a solar seed population. This implies some other source of suprathermal He in the inner heliosphere.

[25] We consider interstellar pickup He^{+} to be the prime candidate for the source population for the reported suprathermal He^{+}. Pickup ions are known to be efficiently accelerated in compressive and turbulent regions of the heliosphere [*Gloeckler et al.*, 1994; *Schwadron et al.*, 1996], where they can reach sufficient energies to effectively participate in shock acceleration or an injection mechanism such as multiple reflected ions [*Rice et al.*, 2000] or shock surfing [*Lee et al.*, 1996]. The two processes are essentially the same. The source of the freshly ionized neutral He could be interstellar neutral He [*Möbius et al.*, 1985] or inner source He [*Gloeckler et al.*, 2000]. Interstellar neutral helium penetrates deeply into the heliosphere, and during solar activity minimum conditions it is ionized predominantly around 0.5 AU. This is illustrated in Figure 13, which shows the fluxes of interstellar pickup He for various solar activities. The dashed curve is for solar activity minimum and peaks around 0.5 AU, while the dash-dotted curve (for solar activity maximum) peaks around 2 AU, reflecting the higher EUV flux that photoionizes the inflowing neutral He. Under normal interplanetary conditions, photoionization is the dominant ionization process for neutral He. Interstellar pickup He contributes significantly to the suprathermal pickup He population under normal conditions [*Hilchenbach et al.*, 1999].

[26] In the presence of IP shocks or other disturbances, electron-impact ionization can contribute significantly if the densities of high-energy electrons (predominantly halo energies) are sufficiently high. The strong shock driven by the ICME observed on DOY 120 was associated with very high solar wind proton densities (ACE level II data, http://www.srl.caltech.edu/ACE/ASC/). Because of charge neutrality, the electron density must have been similarly enhanced. The shock not only compressed the interplanetary medium but it also heated it, as is always the case. Under normal conditions, electron-impact ionization only contributes ~10% to the total ionization of He [*Rucinsky et al.*, 1996]. Scaling this contribution with the inferred electron density at and trailing the shock, and considering the fact that the electrons must also have been heated considerably by the shock, we arrive at the conclusion that the ionization rates for helium during period A must have been at least as high as they are during solar activity maximum, i. e., nearly a factor of 2 or more higher than during the preceding and following time periods. Studying a sample of four shocks, *Isenberg and Feldman* [1995] found that the electron-impact ionization rate β varies upstream of a shock from 0.4 to 7 (10^{-8} s^{-1}) and

downstream from 6.7 to 141 (10^{-8} s^{-1}) compared to the average ionization rate of 1.07 X,10^{-7} s^{-1}*Rucinsky et al.* [1996]. Thus the compression and heating produces significant increases in the electron-impact ionization rate downstream and possibly upstream of a shock that can ionize interstellar atoms at rates matching or exceeding the photoionization or charge exchange rate. Because the loss rates for He were not enhanced prior to the time period investigated, this enhanced ionization must have resulted in a considerable increase in the number of freshly ionized pickup He^{+}.

[27] The variability of He^{+} could be explained by the variability of the electron-impact ionization rate, which depends strongly on the strength of the shock. Under favorable conditions, such as the ones present at the beginning of the May 1998 events, interstellar or inner source pickup He may be an important reservoir of suprathermal particles that are available for acceleration to higher energies. At larger distances from the Sun, the relative difference in time available for acceleration will be smaller, and therefore the accelerated pickup ions will be also observed at higher energies, comparable to those of He^{++}. The relative contribution of inner source and interstellar He can, in principle, be estimated from abundances of other inner source pickup ions such as O, Mg, and Si. For these elements we expect no interstellar contributions. Assuming solar wind abundances for these elements relative to He, the interstellar contribution could easily be determined.

[28] Charge states provide information about the source temperature and the acceleration and propagation of energetic particles. In gradual events the ionization states of energetic particles remain similar to the source plasma of the corona or the solar wind [*Hovestadt et al.*, 1981], while in impulsive events, substantially higher mean charge states ($\sim$14 for Si, $\sim$20 for Fe) are observed [*Klecker et al.*, 1984; *Luhn et al.*, 1987]. Measurements during the gradual events of September–October 1989 in the range 200–600 MeV amu^{-1} [*Tylka et al.*, 1995] and during the two gradual SEP events of October/November 1992 in the ranges 0.5–5 MeV amu^{-1} [*Mason et al.*, 1995] and $\sim$15–70 MeV amu^{-1} [*Leske et al.*, 1995] exhibited a mean ionic charge state of Fe in the range 11–15. Little or no additional stripping is assumed to occur during the acceleration to higher energies. However, in some large SEP events, significant energy dependence of mean ionic charge states of heavy ions is observed. In the two large SEP events in October/November 1992 an increase in the mean ionic charge state of Fe from 11 at 0.3 MeV amu^{-1} to 16 at 30 MeV amu^{-1} was seen [*Oetliker et al.*, 1997]. During the 6 November 1997 SEP event, measurements by instruments on ACE in the energy range $\sim$0.2–1 MeV amu^{-1} [*Möbius et al.*, 1999b], and inferred in the range 12–60 MeV amu^{-1} [*Cohen et al.*, 1999a, 1999b], and independently determined up to 50 MeV amu^{-1} with the polar-orbiting Solar Anomalous and Magnetospheric Particle Explorer (SAMPEX) using the geomagnetic cutoff technique [*Mazur et al.*, 1999], showed an increase of the mean ionic charge states of Si and Fe with increasing energy. The unusually strong energy dependence of the Fe charge states has been explained by stripping of the ions after acceleration, assuming that the shock begins sufficiently low in the corona [*Reames et al.*, 1999]. Another explanation for this behavior may be found in the work of *Forman and Webb* [1985], where energy spectra are described as exponentials in $-v^2 \cdot A/Q$ due to particle escape from finite acceleration volume, and in the work of *Jokipii* [1987], where it is stated that ions gain a significant fraction of their energy in the motional electric field of the shock wave. Nevertheless, the low mean ionic charge states of Fe in both energy ranges and the small Fe/O ratio observed by (H)STOF during event I in the suprathermal energy range, also seen at higher energies [*Klecker et al.*, 2000], are typical for large gradual events. The very unusual charge states of the heavy elements observed in the solar wind in the second half and trailing plasma of the 2–3 May CME (event II) [*Gloeckler et al.*, 1999] are also observed in the accelerated particles. Measurements of Fe charge states with SEP and solar wind instruments suggest the presence of three separate iron populations, within and just outside the magnetic cloud [*Popecki et al.*, 2000]. With STOF we observed a broad Fe charge state distribution with a mean ionic charge state that was two charges higher in the higher energy range than in the low energy range. During event IV, *Popecki et al.* [1999] investigated the temporal variation of the mean ionic charge state of Fe at higher energies. They found a contribution of two populations: one with higher charge states from an impulsive event at the onset of event III and one with lower charges states from a gradual event which became more prominent later in the event. Thus event IV has both impulsive and gradual characteristics. The suprathermal particles observed in event IV show a behavior similar to that in event II. The mean ionic charge state increases from $\sim$9 in the lower energy range to $\sim$11 in the higher energy range. Therefore the energy dependence observed in the suprathermal energy range during events II and IV may be a result of the presence of Fe populations of different origin. The time around and after the strong IP discontinuity on 4 May, which accelerated a large number of particles to higher energies, exhibited a wide charge state distribution of Fe in the energy range 0.18–0.44 MeV amu^{-1} with a mean charge state of 14.6 [*Möbius et al.*, 1999a]. This is also seen in the suprathermal energy range as observed with STOF. In Figure 14 we show the evolution of the Fe charge states in the two energy ranges during event III. The wide distribution in the lower energy range during period H shows a peak in the range Fe^{9+}–Fe^{13+} and a second one in the range Fe^{15+}–Fe^{17+}. During the periods I and J the lower charge state component decreases, and the distribution becomes asymmetric with a peak around Fe^{16+}. This observation may indicate the presence of two particle populations, one locally accelerated with low and high charge states and one with higher charge states possibly coming from the impulsive event observed optically by LASCO on 2 May. Another possibility has been investigated by *Neukomm and Bochsler* [1996]. These authors considered a plasma that is initially heated to high temperatures and subsequently cooled in a nonequilibrium situation. Because of the low recombination of the neon-like Fe^{16+}, this ion essentially acts as a bottleneck for the recombination of Fe to lower charge states. Those ions that do recombine then establish an equilibrium distribution around Fe^{9+}. This scenario can

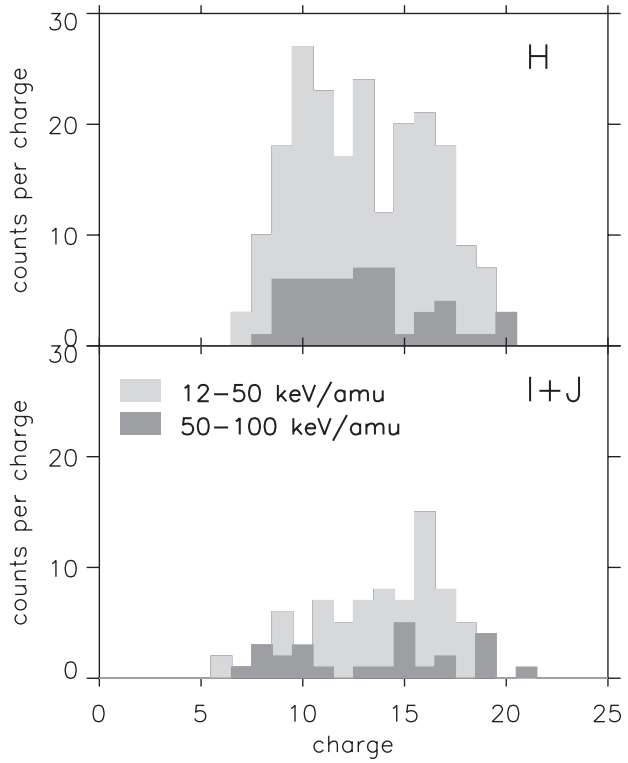

Figure 14. The evolution of the Fe charge states in the two energy ranges during event III.

explain the bimodal charge state distribution of Fe without taking recourse to a mixing of multiple populations.

6. Conclusions

[29] In this work we reported measurements of the composition of interplanetary suprathermal particles in the energy range 10–4000 keV amu^{-1} for the unusual time period of 29 April to 8 May 1998. We found a strong enhancement of He^+ in the suprathermal energy range during the first half of event I. In contrast, the unusually high He^+ abundance in the solar wind associated with the 2–3 May CME [*Gloeckler et al.*, 1999; *Skoug et al.*, 1999] was not observed by STOF. This is a strong indication that the suprathermal He^+ particles are not accelerated out of the solar wind. We consider interstellar pickup He^+ to be the prime candidate for the source population for the reported suprathermal He^+. The low mean ionic charge states of Fe in both energy ranges and the small Fe/O ratio observed by (H)STOF during event I in the suprathermal energy range are typical for large gradual events. The energy dependence of the Fe charge states observed during event II and event III may be a result of either the presence of different iron populations or of the thermal history of the accelerated material or of charge-dependent acceleration and leakage from the acceleration volume. The temporal variations of Fe/CNO and He/CNO during event III indicate a stronger confinement of low-rigidity particles at the acceleration site. These observations greatly extend the energy range in which particles associated with this time period have been measured. We have identified interstellar pickup ions as a possible important nonsolar seed population and described the composition of the suprathermal particles. These particles are prime candidates for the seed population for acceleration to solar energetic particle energies in gradual events.

Appendix A: Data Analysis

[30] In this appendix we describe the principle of the analysis that is based on the most detailed data produced by (H)STOF, the so-called pulse height analysis (PHA) words. They consist of the time of flight, τ, the energy measured in the solid-state detector, E_{SSD}, the position on the microchannel plates and the solid-state detector, the gain flag of the solid-state detector, and the energy per charge, E/q, of an ion when entering the instrument. By using the position sensing of the microchannel plates and the position determination of the solid-state pixel detector, the distinction between STOF and HSTOF events can be made, and events in high-background solid-state detector pixels can be rejected. This leads to an improved signal-to-noise ratio.

A1. Extraction

[31] By combination of the E/q information, the time of flight, τ, and the residual energy measured in the solid-state detector, E_{SSD}, the mass, m, and the initial energy, E, and in addition for STOF the mass per charge, m/q, and the charge, q, of an incoming ion can be determined unambiguously.

[32] With both STOF and HSTOF the mass is determined by a function of τ and E_{SSD}:

$$m = 2 \cdot \left(\frac{\tau}{d}\right)^2 \cdot (E_{\mathrm{SSD}} + \Delta E_{\mathrm{SSD}}), \tag{A1}$$

where d denotes the length of the time-of-flight unit and E_{SSD} denotes the energy loss in the dead layer of the solid-state detector. Using flight data, we found that ΔE_{SSD} can be approximated by

$$\frac{E_{\mathrm{SSD}}}{E_0}[\%] = 100 - 220 \cdot \left(\frac{E_0}{m}[keV\ amu^{-1}]\right)^{-0.45}, \tag{A2}$$

where E_0/m is the energy per mass after the foil corresponding to τ. Since the STOF entrance system selects the incoming ions according to their energy per charge, E/q, the mass per charge is determined by

$$\frac{m}{q} = 2 \cdot \left(\frac{\tau}{d}\right)^2 \cdot \left(\frac{E}{q} - \frac{\Delta E_{\mathrm{foil}}}{q}\right), \tag{A3}$$

which combined with equation (A1) gives the charge, q, of an ion. Its initial energy is then determined by

$$E = \frac{E}{q} \cdot q. \tag{A4}$$

For heavy ions the energy loss in the foil, ΔE_{foil}, is approximated by 5% of the initial energy. Note that in the energy range of STOF the mass-per-charge measurement is more precise than the measurement of the mass. The initial energy, E, can also be written as a function of E_{SSD}:

$$E = E_{\mathrm{SSD}} + \Delta E_{\mathrm{SSD}} + \Delta E_{\mathrm{foil}}. \tag{A5}$$

In the case of HSTOF the energy loss in the silicon-lexan-carbon foil is calculated with software based on Transport of Ions in Matter (TRIM) simulations.

A2. Efficiencies

[33] Both STOF and HSTOF measure the differential fluxes in particles/(cm^2 sr keV/amu)]:

$$\frac{dJ}{dE} = \frac{\text{counts}}{\text{keV amu}^{-1}} \cdot \frac{1}{p_{E/q} \cdot \eta_T \cdot g}, \tag{A6}$$

where η_T is the detection efficiency, g is the geometrical factor of the entrance system, $p_{E/q}$ is the probability to get through that E/q step. We estimate the systematic uncertainty in $\frac{dJ}{dE}$ to be $\sim$10%. To determine the elemental abundance ratios only η_T needs to be considered, since g and $p_{E/q}$ are constant and thus cancel in ratios. Value $p_{E/q}$ is the E/q step width divided by the FWHM of the E/q distribution. The triple coincidence efficiency, η_T, is defined as $\eta_T = \eta_1 \cdot \eta_2 \cdot p_E$, i. e., as the probability that an ion generates a start and a stop signal and its energy is measured in the solid-state detector. The scattering of the ions in the entrance foil leads to a variation of the measured time of flight, but it does not affect the detection efficiency. The scattering angles for the energies reported here are small, and the area of the solid-state detector is large compared to the variation in the time-of-flight path. Because the background is mainly UV induced and low during the period investigated and because the particle fluxes were not high enough to bring (H)STOF anywhere near saturation, dead-time effects did not reduce the detection efficiency. Value p_E depends on the energy threshold of the solid-state detector and on the residual energy of the ion after passage through the carbon foil and the dead layer of the solid-state detector. An ion generates a start and a stop signal with the probabilities η_1 and η_2. These depend on the thickness of the foil, s, the mean number of secondary electrons, n_{foil} and n_{SSD}, emitted by the foil and the Al_2O_3 layer of the solid-state detector as evaluated by TRIM, respectively, and on the probability that a secondary electron triggers a start or a stop signal on the microchannel plate detector, ϵ_1 and ϵ_2. The secondary electron numbers, n_{foil} and n_{SSD}, depend on the ion's energy and its atomic number Z. The start and stop efficiencies used in this work, η_1 and η_2, are then calculated as described by *Hefti* [1997]:

$$\eta_1 = 1 - \exp[-t \cdot \epsilon_1 \cdot n_{\text{foil}}] \tag{A7}$$

$$\eta_2 = t' \cdot (1 - \exp[-t \cdot \epsilon_2 \cdot n_{\text{SSD}}]). \tag{A8}$$

Value t denotes the probability that an ion passes the grids of the electron mirror, and t' denotes the ion optical trasmission. The values for t, t', ϵ_1, and ϵ_2 derived from calibration data are taken from *Hefti* [1997]. The mean numbers of secondary electrons, n_{foil} and n_{SSD}, are calculated with software based on TRIM simulations. Owing to the accumulated UV fluence, the microchannel plate efficiencies ϵ_1 and ϵ_2 have diminished from their calibrated values to some smaller, unknown values. We multiplied the expression in the exponent in equations (A7) and (A8) by factors $c_1(Z) < 1$ and $c_2(Z) < 1$ to account this degredation. We found that the start and stop efficiencies η_1 and η_2 calculated with reduced values for ϵ_1 and ϵ_2 remain roughly (±10%) constant over the energy range 0.05–1 MeV amu^{-1} for all elements. Within ±10% we can approximate the detection efficiency by $\eta_T = C(Z) \cdot \eta_1 \cdot \eta_2 \cdot p_E$, where $C(Z) < 1$. This greatly simplifies the subsequent analysis without introducing any serious uncertainty. We account for this approximation in the final uncertainties given in the text or in the tables. Weighting the detection efficiencies with the observed fluxes further reduces the uncertainties because the dominant contribution to the flux comes from a small range in energy over which the approximation is better. In order to derive elemental abundance ratios we determined the element-dependent overall normalization factor C for H, He, CNO, and Fe by normalizing the He/H, He/CNO, and Fe/CNO ratios to the values given in by, for example, *Reames* [1999] (He/H = 0.036 ± 005, He/CNO = 36 ± 2, and Fe/CNO = 0.084 ± 0.003) during a reference period in their respective energy ranges (see Table 1).

A3. Reference Period

[34] We selected the 5 days (DOY 115–119) just before the onset of event I on DOY 120 as a reference period. No STP events or IP shocks occurred during this time. The background was low and limited to the low-energy channels. We normalized the He/H ratio measured over this time to the average coronal abundance ratios:

$$\left(\frac{\text{He}}{\text{H}}\right)_{\text{ref}} \cdot \frac{C_{\text{H}}}{C_{\text{He}}} = \left(\frac{\text{He}}{\text{H}}\right)_{\text{cor}}, \tag{A9}$$

where index "ref" indicates our measurement during the reference period and index "cor" indicates the coronal values [*Reames*, 1999]. Since we base our arguments on variations of elemental and charge state ratios, their absolute value is not important. By setting C_{H} to 1, C_{He} can be determined. C_{CNO} and C_{Fe} are then calculated successively by applying equation (A9) to He/CNO and Fe/CNO. We obtained the values 0.33 (C_{He}), 0.57 (C_{CNO}), and 0.83 (C_{Fe}). Again, we stress that we have based our argumentation in the paper on short-time variations of the abundance ratios. These variations are not affected by the long-term degradation of the efficiency of the microchannel plates that makes these renormalizations necessary.

Appendix B: Model

[35] In this appendix we give a short description of the efficiency model of the STOF section. It includes E/q acceptance of the entrance E/q analyzer, its E/q stepping, energy loss and energy straggling in the carbon foil, the time-of-flight measurement, and the energy measurement in the solid-state detector. The angular acceptance of the entrance system and the angular scattering in the carbon foil, which both lead to a variation of the path length and the measured time of flight, are neglected. The triple coincidence rate is calculated as described in section A2. The E/q acceptance is approximated by a Gaussian centered on the E/q value of the E/q step with a FWHM of $0.095 \cdot E/q$. The average energy loss in the carbon foil is approximated by 5% of the initial energy. The asymmetric time-of-flight

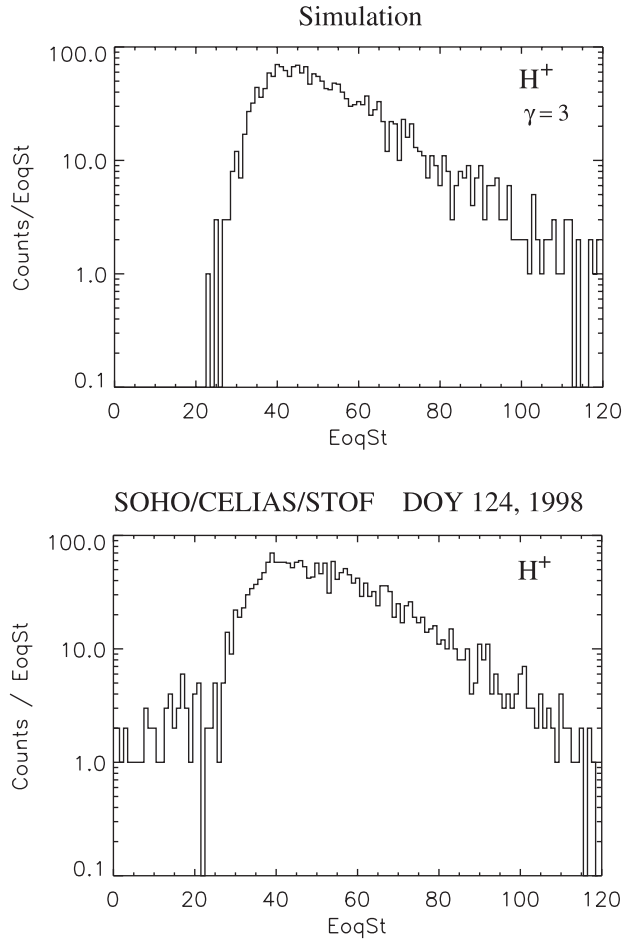

Figure B1. Comparison of (top) the simulated spectrum with (bottom) the measured spectrum on DOY 124, showing a good agreement.

distribution after the carbon foil can be described by the expression given by *Luhn* [1982]:

$$N(\tau) \sim \begin{cases} \exp\left[-\frac{(\tau-\overline{\tau})^2}{2\sigma^2}\right] & ;\tau \le \overline{\tau} \\ \exp\left[\left[-\frac{(\tau-\overline{\tau})^2}{2\sigma^2}\right]\right. & \\ \quad \left.\cdot\left[1+\left(\frac{\tau-\overline{\tau}}{2\sigma^2\delta}\right)^2\right]^{-0.5}\right] & ;\tau \ge \overline{\tau} \end{cases} \quad \text{(B1)}$$

where $\overline{\tau}$ denotes the time of flight corresponding to the average energy after the carbon foil, and τ is the actual time of flight after the foil. The standard deviation σ is approximated by 2% of the time of flight before the foil, and δ is set to 1.5. In addition, our model includes effects due to instrumental dead times and effects due to the imperfect detection probabilities. A measured time of flight can belong to a single event or to a two-particle event. In the first case the start and stop signal is generated by the same particle. The measured time of flight corresponds to its energy after the foil. In the second case a first ion enters the time-of-flight section, generating a start signal but no stop, while a second ion triggers the stop pulse, and vice versa. The measured time of flight is therefore too long or too short, respectively. These accidental counts result in a strongly flux dependent background that extends over the entire time-of-flight domain of STOF. The energy threshold of the solid-state detector is 55 keV with a one standard deviation width of 5 keV. In our model a particle energy is measured with a probability that mimics the energy response of the solid-state detector. Figure B1 shows the result of one of our instrument simulations compared with the H^+ spectrum measured on DOY 124. For the simulation we assumed a spectral index $\gamma = 3$ and varied the total particle flux to obtain good agreement. The simulated events are generated with a Monte Carlo code. The particles detected in the low E/q steps are probably caused by UV and not by accidental counts and therefore cannot be expected to be reproduced with our model. Moreover, they account for only a minuscule fraction of the detected particles.

[36] **Acknowledgments.** CELIAS is a joint effort of five hardware institutions under the direction of the Max-Planck-Institut für extraterrestrische Physik (prelaunch) and the University of Bern (postlaunch). The Max-Planck-Institut für extraterrestrische Physik is the prime hardware institution for (H)STOF. The University of Bern provided the entrance system. The DPU was provided by the Technical University of Braunschweig. This work was supported by the Swiss National Science Foundation.

[37] Michel Blanc thanks Donald V. Reames and another referee for their assistance in evaluating this paper.

References

Chotoo, K., et al., The suprathermal seed population for corotating interaction region ions at 1 AU deduced from composition and spectra of H^+, He^{++}, and He^+ observed on Wind, *J. Geophys. Res.*, *105*, 23,107–23,122, 2000.

Cohen, C. M. S., E. R. Christian, A. C. Cummings, R. A. Leske, R. A. Mewaldt, P. L. Slocum, E. C. Stone, T. T. von Rosenvinge, and M. E. Wiedenbeck, New measurements of solar particle events enriched in heavy ions, edited by D. Kieda, M. Salamon, and B. Dingus, *Conf. Pap. Int. Cosmic Ray Conf. 26th*, 244–247, 1999a.

Cohen, C. M. S., A. C. Cummings, R. A. Leske, R. A. Mewaldt, E. C. Stone, B. L. Dougherty, M. E. Wiedenbeck, E. R. Christian, and T. T. von Rosenvinge, Inferred charge states of high energy solar particles from the Solar Isotope Spectrometer on ACE, *Geophys. Res. Lett.*, *26*, 149–152, 1999.

Ellison, D. C., and R. Ramaty, Shock acceleration of electrons and ions in solar flares, *Astrophys. J.*, *298*, 400–408, 1985.

Fenimore, E. E., Solar wind flows associated with hot heavy ions, *Astrophys. J.*, *235*, 245–257, 1980.

Forman, M. A., and G. M. Webb, Acceleration of energetic particles, in *Collisionless Shocks in the Heliosphere: Reviews of Current Research*, *Geophys. Monogr. Ser.*, vol. 35, edited by B. T. Tsurutani and R. G. Stone, pp. 91–114, AGU, Washington D. C., 1985.

Gloeckler, G., J. Geiss, E. C. Roelof, L. A. Fisk, F. M. Ipavich, K. W. Ogilvie, L. J. Lanzerotti, R. von Steiger, and B. Wilken, Acceleration of interstellar pickup ions in the disturbed solar wind observed on ULYSSES, *J. Geophys. Res.*, *99*, 17,637–17,643, 1994.

Gloeckler, G., et al., Investigation of the composition of solar and interstellar matter using solar wind and pickup ion measurements with SWICS and SWIMS on the ACE spacecraft, *Space Sci. Rev.*, *86*, 497–539, 1998.

Gloeckler, G., S. Hefti, T. H. Zurbuchen, N. A. Schwadron, L. A. Fisk, F. M. Ipavich, J. Geiss, P. Bochsler, and R. F. Wimmer-Schweingruber, Unusual composition of the solar wind in the 2–3 May 1998 CME observed with SWICS on ACE, *Geophys. Res. Lett.*, *26*, 157–160, 1999.

Gloeckler, G., L. A. Fisk, J. Geiss, N. A. Schwadron, and T. H. Zurbuchen, Elemental composition of the inner source pickup ions, *J. Geophys. Res.*, *105*, 7459–7464, 2000.

Gosling, J. T., The solar flare myth, *J. Geophys. Res.*, *98*, 18,937–18,949, 1993.

Hefti, S., Solar wind freeze-in temperatures and fluxes measured with SOHO/CELIAS/CTOF and calibration of the CELIAS sensors, Ph.D. thesis, Univ. of Bern, Switzerland, 1997.

Hilchenbach, M., H. Grünwaldt, R. Kallenbach, B. Klecker, H. Kucharek, F. M. Ipavich, and A. B. Galvin, Observations of suprathermal helium at 1 AU: Charge states in CIRs, in *Solar Wind Nine*, edited by S. R. Habbal et al., *AIP Conf. Proc.*, *471*, 605–608, 1999.

Ho, G. C., D. C. Hamilton, G. Gloeckler, and P. Bochsler, Enhanced solar wind $^3He^{2+}$ associated with coronal mass ejections, *Geophys. Res. Lett.*, *27*, 309–312, 2000.

Hovestadt, D., G. Gloeckler, H. Höfner, B. Klecker, C. Y. Fan, L. A. Fisk, F. M. Ipavich, J. J. Gallagher, and M. Scholer, Direct observation of

abundances of energetic He, C,O and Fe emitted in solar flares, *Adv. Space Res.*, *1*(3), 61–64, 1981.
Hovestadt, D., et al., ELIAS: Charge, element and isotope analysis system for SOHO, *Sol. Phys.*, *162*, 441–481, 1995.
Ipavich, F. M., A. B. Galvin, G. Gloeckler, D. Hovestadt, S. J. Bame, B. Klecker, M. Scholer, L. A. Fisk, and C. Y. Fan, Solar wind Fe and CNO measurements in high-speed flows, *J. Geophys. Res.*, *91*, 4133–4141, 1986.
Isenberg, P. A., and W. C. Feldman, Electron-impact ionization of interstellar hydrogen and helium at interplanetary shocks, *Geophys. Res. Lett.*, *22*, 873–875, 1995.
Jokipii, J. R., Rate of energy gain and maximum energy in diffusive shock acceleration, *Astrophys. J.*, *313*, 842–846, 1987.
Kahler, S. W., Solar flares and coronal mass ejections, *Annu. Rev. Astron. Astrophys.*, *30*, 113–141, 1992.
Kahler, S. W., Injection profiles of solar energetic particles as functions of coronal mass ejection heights, *Astrophys. J.*, *428*, 837–842, 1994.
Kahler, S. W., Coronal mass ejections and solar energetic particles, in *High Energy Solar Physics*, edited by R. Ramaty, N. Mandzhavidze, and X.-M. Hua, *AIP Conf. Proc.*, *374*, 61–77, 1996.
Klecker, B., D. Hovestadt, G. Gloeckler, F. M. Ipavich, M. Scholer, C. Y. Fan, and L. A. Fisk, Direct determination of the ionic charge distribution of helium and iron in ^{3}He-rich solar energetic particle events, *Astrophys. J.*, *281*, 458–462, 1984.
Klecker, B., E. Möbius, M. A. Popecki, L. M. Kistler, A. Bogdanov, A. B. Galvin, D. Heirtzler, D. Morris, and D. Hovestadt, The ionic charge state composition of CME related solar energetic particle events as observed with SEPICA onboard ACE, edited by D. Kieda, M. Salamon, and B. Dingus, *Conf. Pap. Int. Cosmic Ray Conf. 26th*, 83–86, 1999.
Klecker, B., et al., Comparison of ionic charge states of energetic particles with solar wind charge states in CME related events, in *Acceleration and Transport of Energetic Particles Observed in the Heliosphere*, edited by R. A. Mewaldt et al., *AIP Conf. Proc.*, 528, 135–138, 2000.
Lee, M. A., V. D. Shapiro, and R. Z. Sagdeev, Pickup ion energization by shock surfing, *J. Geophys. Res.*, *101*, 4777–4789, 1996.
Leske, R. A., J. R. Cummings, R. A. Mewaldt, E. C. Stone, and T. T. von Rosenvinge, Measurements of the ionic charge states of solar energetic particles using the geomagnetic field, *Astrophys. J.*, *425*, L149–L152, 1995.
Luhn, A., Flugzeitspektrometermessung von Umladung und Energieverlust in Kohlenstoffolien an Ionen im Energiebereich von 10 bis 300 keV, Master's thesis, Tech. Univ. München, Germany, 1982.
Luhn, A., B. Klecker, D. Hovestadt, and E. Möbius, The mean charge of silicon in ^{3}He-rich solar flares, *Astrophys. J.*, *317*, 951–955, 1987.
Mason, G. M., G. Gloeckler, and D. Hovestadt, Temporal variations of the nucleonic abundances in solar flare energetic particle events, I, Well-connected events, *Astrophys. J.*, *267*, 844–862, 1983.
Mason, G. M., J. E. Mazur, M. D. Looper, and R. A. Mewaldt, Charge states of solar energetic particles observed with SAMPEX, *Astrophys. J.*, *425*, 901–911, 1995.
Mason, G. M., et al., Ultra-Low-Energy Isotope Spectrometer (ULEIS) for the ACE spacecraft, *Space Sci. Rev.*, *86*, 409–448, 1998.
Mason, G. M., J. E. Mazur, and J. R. Dwyer, ^{3}He enhancements in large solar energetic particle events, *Astrophys. J.*, *525*, L133–L136, 1999.
Mazur, J. E., G. M. Mason, M. D. Looper, R. A. Leske, and R. A. Mewaldt, Charge states of solar energetic particles using the geomagnetic cutoff technique: SAMPEX measurements in the 6 November 1997 solar particle event, *Geophys. Res. Lett.*, *26*, 173–176, 1999.
McComas, D. J., S. J. Bame, P. Barker, W. C. Feldman, J. L. Phillips, P. Riley, and J. W. Griffee, Solar Wind Electron Proton Alpha Monitor (SWEPAM) for the Advanced Composition Explorer, *Space Sci. Rev.*, *86*, 563–612, 1998.
Möbius, E., D. Hovestadt, B. Klecker, M. Scholer, and G. Gloeckler, Direct observation of He^+ pick-up ions of interstellar origin in the solar wind, *Nature*, *318*, 426–429, 1985.
Möbius, E., et al., Solar Energetic Particle Ionic Charge Analyzer (SEPICA) and the Data Processing Unit (S3DPU) for SWICS, SWIMS and SEPICA, Space Sci. Rev., *86*, 449–485, 1998.
Möbius, E., B. Klecker, M. A. Popecki, A. B. Galvin, D. Heirtzler, D. Morris, C. Siren, A. Bogdanov, and D. Hovestadt, Variation of ionic charge states between solar energetic particle events as observed with ACE SEPICA, edited by D. Kieda, M. Salamon, and B. Dingus, *Conf. Pap. Int. Cosmic Ray Conf. 26th*, 87–90, 1999a.
Möbius, E., et al., The solar energetic particle event, *Geophys. Res. Lett.*, *26*, 145–148, 1999b.
Müller-Mellin, R., et al., COSTEP: Comprehensive Suprathermal and Energetic Particle Analyser, *Sol. Phys.*, *162*, 483–504, 1995.
Neukomm, R. O., and P. Bochsler, Diagnostics of closed magnetic structures in the solar corona using charge states of helium and of minor ions, *Astrophys. J.*, *465*, 462–472, 1996.
Ng, C. K., D. V. Reames, and A. J. Tylka, A model for the evolution of the elemental abundances of solar energetic particles, *Conf. Pap. Int. Cosmic Ray Conf. 26th*, 147–150, 1999.
Oetliker, M., B. Klecker, D. Hovestadt, G. M. Mason, J. E. Mazur, R. A. Leske, R. A. Mewaldt, J. B. Blake, and M. D. Looper, The ionic charge states of solar energetic particles with energies of 0.3–70 MeV per nucleon, *Astrophys. J.*, *477*, 495–501, 1997.
Popecki, M. A., et al., Time profiles of ionic charge state for rapidly rising solar activity periods, edited by D. Kieda, M. Salamon, and B. Dingus, *Conf. Pap. Int. Cosmic Ray Conf. 26th*, 139–142, 1999.
Popecki, M. A., et al., Simultaneous high Fe charge state measurement by solar energetic particle and solar wind instruments, in *Acceleration and Transport of Energetic Particles Observed in the Heliosphere*, edited by R. A. Mewaldt et al., *AIP Conf. Proc.*, *528*, 139–142, 2000.
Reames, D. V., Energetic particles from impulsive solar flares, *Astrophys. J. Suppl. Ser.*, *73*, 235–251, 1990.
Reames, D. V., Non-thermal particles in the interplanetary medium, *Adv. Space Res.*, *13*(9), 331–339, 1993.
Reames, D. V., Particle acceleration at the Sun and in the heliosphere, *Space Sci. Rev.*, *90*(3–4), 413–491, 1999.
Reames, D. V., C. K. Ng, and A. J. Tylka, Energy-dependent ionization states of shock-accelerated particles in the solar corona, *Geophys. Res. Lett.*, *26*, 3585–3588, 1999.
Reames, D. V., C. K. Ng, and A. J. Tylka, Initial time dependence of abundances in solar energetic particle events, *Astrophys. J.*, *581*, L83–L86, 2000.
Rice, W. K. M., G. P. Zank, J. D. Richardson, and R. B. Decker, Ion injection and shock acceleration in the outer heliosphere, *Geophys. Res. Lett.*, *27*, 509–512, 2000.
Rucinsky, D., A. C. Cummings, G. Gloeckler, A. J. Lazarus, E. Möbius, and M. Witte, Ionization processes in the heliosphere: Rates and methods of their determination, *Space Sci. Rev.*, *78*, 73–84, 1996.
Russell, C. T., G. Le, P. Chi, X.-W. Zhou, J.-H. Shue, S. M. Petrinek, P. Song, F. R. Fenrich, and J. G. Luhmann, The extreme compression of the magnetosphere on May 4, 1998, as observed by the Polar spacecraft, *Adv. Space Res.*, *25*(7–8), 1369–1375, 2000.
Schwadron, N. A., L. A. Fisk, and G. Gloeckler, Statistical acceleration of interstellar pick-up ions in co-rotating interaction regions, *Geophys. Res. Lett.*, *23*, 2871–2874, 1996.
Schwenn, R., H. Rosenbauer, and K.-H. Mühlhäuser, Singly-ionized helium in the driver gas of an interplanetary shock wave, *Geophys. Res. Lett.*, *7*, 201–204, 1980.
Skoug, R. M., et al., A prolonged He^+ enhancement within a coronal mass ejection in the solar wind, *Geophys. Res. Lett.*, *26*, 161–164, 1999.
Stone, E. C., et al., Solar Isotope Spectrometer for the Advanced Composition Explorer, *Space Sci. Rev.*, *86*, 357–408, 1998.
Torsti, J., et al., Energetic Particle Experiment ERNE, *Sol. Phys.*, *162*, 505–531, 1995.
Tylka, A. J., P. R. Boberg, J. J.-H. Adams, L.-P. Beahm, W. F. Dietrich, and T. Kleis, The mean charge state of solar energetic Fe ions above 200 MeV per nucleon, *Astrophys. J.*, *444*, L109–L113, 1995.
Tylka, A. J., D. V. Reames, and C.-K. Ng, Observations for systematic temporal evolution in elemental composition during gradual solar energetic particle events, *Astrophys. J.*, *26*(14), 2141–2144, 1999.
Vasyliunas, V. M., and G. L. Siscoe, On the flux and the energy spectrum of interstellar ions in the solar system, *J. Geophys. Res.*, *81*, 1247–1252, 1976.
von Rosenvinge, T. T., C. M. S. Cohen, E. R. Christian, A. C. Cummings, R. A. Leske, R. A. Mewaldt, P. I. Slocum, E. C. Stone, and M. E. Wiedenbeck, Time variations of solar energetic particle abundances observed by the ACE spacecraft, edited by D. Kieda, M. Salamon, and B. Dingus, *Conf. Pap. Int. Cosmic Ray Conf. 26th*, 131–134, 1999.
Zwickl, R. D., J. R. Asbridge, S. J. Bame, W. C. Feldman, and J. T. Gosling, He^+ and other unusual ions in the solar wind: A systematic search covering 972–980, *J. Geophys. Res.*, *87*, 7379–7388, 1982.

K. Bamert, R. F. Wimmer-Schweingruber, and P. Wurz, Physikalisches Institut, Universität Bern, Sidlerstrasse 5, CH-3012 Bern, Switzerland. (karin.bamert@soho.unibe.ch; robert.wimmer@phim.unibe.ch)
A. Bogdanov, Institut für Geophysik und Meteorologie, Technische Universität Braunschweig, D-38106 Braunschweig, Germany.
M. Hilchenbach, Max-Planck-Institut für Aeronomie, D-37189 Katlenburg-Lindau, Germany.
R. Kallenbach, International Space Science Institute, Hallerstrasse 6, CH-3012 Bern, Switzerland.
B. Klecker, Max-Planck-Institut für extraterrestrische Physik, D-85740 Garching, Germany.